Atmospheric Environment 111 (2015) 151–160

Contents lists available at ScienceDirect

Atmospheric Environment

journal homepage: www.elsevier.com/locate/atmosenv

Source characterization of carbon monoxide and ozone over the Northwestern Pacific in summer 2012

Keyhong Park, Tae Siek Rhee*

Division of Polar Ocean Environment, Korea Polar Research Institute, Incheon 406-840, South Korea

HIGHLIGHTS

- The CO-tagged MOZART4 provides useful insight about the origin and transport of CO.
- The relative importance of biomass burning CO increased in the higher latitudes.
- Over the Bering Sea, the European anthropogenic CO is comparable to the NE Asian's.
- The oceanic CO might be important to understand the MBL CO variations in summer.
- O_3 is mainly formed by photochemistry from CO in the NE Asia region.

ARTICLE INFO

Article history:
Received 9 December 2014
Received in revised form
7 April 2015
Accepted 8 April 2015
Available online 9 April 2015

Keywords:
Carbon monoxide
Ozone
Marine boundary layer
Global chemical transport model
Source composition

ABSTRACT

Carbon monoxide (CO) and ozone (O_3) were continuously measured in the marine boundary layer of the East Sea, the Northwestern Pacific, and the Bering Sea onboard *R/V Araon* in the second halves of July and September of 2012, as a part of the SHIpborne Pole-to-Pole Observations (SHIPPO) program. Depending on the characteristics of each section of the cruise track, up to 66 ppbv and 17 ppbv of CO and O_3 variability were observed, respectively. The O_3/CO ratio suggests that O_3 was dominantly produced by photochemical reactions in the troposphere, although in the northern sections of the cruise track, the ratio likely suggests vertical transport from the free troposphere or the lowermost stratosphere. To analyze the source characteristics and the transport of both trace gases, a tagging technique in a 3-D global chemical transport model (Model for OZone And Related chemical Tracers-4; MOZART-4) was applied. The model reproduced the observations fairly well, and the technique enabled us to characterize the source regions and composition of the observed CO. Anthropogenic emissions from Northeastern Asian countries appeared to be substantial sources of the CO in the southern sections, and biomass burning in Siberia was an important source of the CO observed in the northern sections of the cruise track. Long-range transport of anthropogenic CO emissions was distinct over the Bering Sea, where the comparable contributions from North America, Northeast Asia, and Europe were identified. Low CO events driven by southern hemispheric invasion were encountered at the southern coast of the Korean peninsula and in the North Pacific at ~50N latitude. The model pointed to a noticeable contribution from the open ocean in the Southern Hemisphere for these events.

1. Introduction

Investigating the variation of sources, sinks, and transport of atmospheric trace gases is essential to understand the atmospheric environment. Because atmospheric carbon monoxide (CO) is a major sink of hydroxyl radicals (OH), it plays an important role in estimating the atmospheric oxidizing capacity (Brenninkmeijer et al., 1999). Additionally, it is closely related to ozone-related chemistry and directly and indirectly contributes to the change of radiative forcing (Crutzen and Zimmermann, 1991; Ehhalt et al., 2001). Large amounts of CO are emitted from the incomplete combustion of fossil fuels in urban areas as well as from biomass burning. Thus, CO has been used as a tracer of anthropogenic pollution and biomass burning plumes (Pfister et al., 2005; Shim et al., 2009).

Atmospheric CO is a complex mixture of various sources and sinks. Major sources of CO include the oxidation of methane (CH_4)

* Corresponding author.
E-mail address: rhee@kopri.re.kr (T.S. Rhee).

http://dx.doi.org/10.1016/j.atmosenv.2015.04.015
1352-2310/

and non-methane hydrocarbons (NMHC) and direct emissions from burning biomass and human activities (fossil fuel and biofuel use) (Duncan et al., 2007). Atmospheric OH removes approximately 90% of the CO in the atmosphere, and the remainder is removed by microbial uptake in the soil (Bergamaschi et al., 2000; Hauglustaine et al., 1998; Sanhueza et al., 1998; Weinstock and Niki, 1972).

Tropospheric O_3 is mainly produced by photochemical reactions in the troposphere, and approximately 10% of O_3 is added by stratosphere–troposphere exchange (Stevenson et al., 2006). O_3 is a primary source of the hydroxyl radicals in the troposphere. It acts as a greenhouse gas, which contributes to global climate change, and is a harmful air pollutant causing adverse health effects (IPCC, 2007). In urban areas and plumes from biomass burning, O_3 is produced from photochemical chain reactions of nitrogen oxides (NO_x) and volatile organic compounds (VOCs). In the free troposphere or remote and unpolluted areas, in the presence of NO_x, photochemical oxidation of CO and CH_4 serves as the major process producing O_3.

Ground-based CO and O_3 measurements are being conducted by numerous independent air quality monitoring programs and global monitoring networks led by the Global Monitoring Division at the National Oceanic and Atmospheric Administration (NOAA GMD) (Novelli et al., 2003) and the Global Atmospheric Watch (GAW) of the World Meteorological Organization (Buchmann et al., 2010). Although some monitoring stations are located in coastal areas, they often observe the continental outflow from polluted point sources. Thus, despite the significance of measuring CO and O_3 to understand photochemical reactions within the marine boundary layer (MBL) (Dickerson et al., 1999; Heard et al., 2006), few observations have been recorded due to limited accessibility and research resources. Space-borne CO and O_3 observations are also available (Edwards et al., 2006; Kim et al., 2013). However, their vertical resolution and relatively long revisit periods do not provide adequate information to investigate changes in the atmospheric chemical environment in the MBL. Thus, direct ship-borne high-resolution observations are essential to understand the photochemical processes in the marine bound layer.

We took advantage of Korean ice breaker *R/V Araon*'s regular visit to the Arctic Ocean and the Southern Ocean under the SHIp-borne Pole-to-Pole Observations (SHIPPO) program, which facilitates high-resolution measurements of atmospheric components, including CO and O_3. We conducted continuous observations along the *R/V Araon*'s route to the Arctic Ocean and during the return to Korea. Here, we analyzed the influence of anthropogenic and biomass burning emissions on the variability of CO and O_3 over the Northwestern Pacific and the Bering Sea. Along with onboard measurements, a 3-D Global Chemical Transport Model (Model for OZone And Related chemical Tracers − 4; MOZART-4) (Emmons et al., 2010) was used to simulate the concentrations of these trace gases and aided in the analysis of the contribution of sources and regional contributions to the atmospheric CO observed along the cruise track.

2. Observations

2.1. Cruises

This study was composed of two research cruises. *R/V Araon* left Incheon, Korea, on July 13, 2012, and arrived at Nome in Alaska, U.S.A., on July 29. After finishing the Arctic survey, she left Nome, Alaska, on September 11 and arrived at Busan, Korea, on September 23. Both cruises covered the East Sea, Northwestern Pacific, and the Bering Sea (Fig. 1).

2.2. Continuous measurements of CO and O_3

The observations of atmospheric CO were made using Off-Axis Integrated Cavity Output Spectroscopy (Off-Axis ICOS: N_2O/CO analyzer; Los Gatos Research, USA) (Arévalo-Martínez et al., 2013; Zellweger et al., 2012). The instrument was set up in a seatainer located on the top of the bridge. A 1.8-m long air inlet chimney, coated with Teflon on the surface, was seated near the right front edge on the top of the seatainer. A Pyrex manifold was located right behind the chimney and in front of the blower. The ambient air entered the air inlet and was ventilated through the manifold at 300 m^3 min^{-1} by the blower. Air samples were withdrawn from the manifold to the cavity cell at ~400 mL min^{-1} by a pump mounted inside the instrument. The cell pressure was maintained at 85 torr. Mean value data were acquired every 10 s. The instrument was calibrated with a standard gas (500(±10) ppb, Scott-Marrin Inc.) once per week. We also analyzed the ambient CO using a gas chromatograph (RGA3, Trace Analytical Co.), which detected the Hg produced by reacting with CO and HgO, to determine whether a drift occurred from the relatively long calibration interval and to verify our high frequency measurement. In the 1-to-1 plot, they provided a robust correlation coefficient ($r^2 = 0.98$) (see Fig. S1). The mean absolute difference ($1/N \times \sum|CO_{RGA} - CO_{LGR}|$) of the concentrations is defined as 3.2 ppbv.

The O_3 concentration was continuously measured using a typical photo-absorption technique (Thermo 49i), and the data were stored every 5 min. The instrument was calibrated at the Korea Research Institute of Standards and Science (KRISS) a few weeks before starting the cruise.

2.3. Identification of ship exhaust

Sudden changes in the CO and O_3 concentrations were probably due to emissions from the ship exhaust. The high frequency (0.1 Hz) CO concentration was used to remove the polluted air recorded in the data according to the following procedure. First, the data acquired when the relative wind speed (with respect to the ship speed) was lower than 2 knots were discarded to avoid potential influence from the stack emission due to local turbulence. When the contaminated air was drawn into the air inlet, the instrument detected high CO with short-term fluctuations. Thus, we only kept the data that had a standard deviation for one minute that was less than 1 ppbv. Finally, when the relative wind direction against the ship's heading was between 180° and 270°, where the ship stack was located from the air inlet, a strict criterion was applied; the data with 1-min standard deviations larger than 0.1 ppbv were rejected. The time window where CO passed this quality control was also applied for O_3 (Fig. S2).

2.4. Transport of air parcels

The Hybrid Single Particle Lagrangian Integrated Trajectory (HYSPLIT) model (Draxler and Hess, 1998) was applied to calculate 5-day backward trajectories of air parcels along the cruise tracks (Fig. 1). The HYSPLIT model was run, with archived NCEP/NCAR reanalysis meteorology (Kistler et al., 2001) at a 2.5° × 2.5° horizontal resolution and 28 vertical sigma levels reaching 10 hPa. Based on this, the cruise tracks were divided into ten air masses (Table 1).

During the July cruise (sections I–V), air parcels were mainly transported over the ocean. The planetary boundary layer height (PBLH) that was obtained by LIDAR during the July cruise was approximately 400 m. Most of the trajectories indicate that the air masses were transported below the PBLH. In section I, we encountered air parcels advected from the South China Sea and

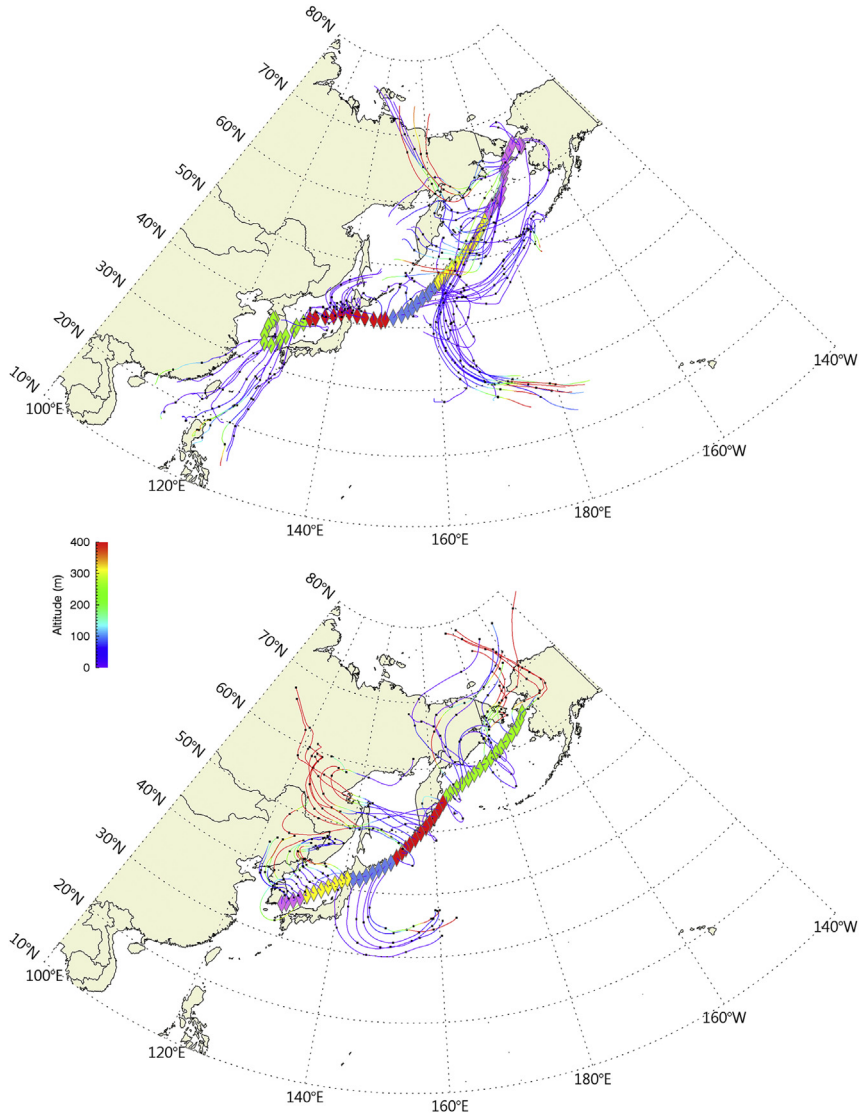

Fig. 1. HYSPLIT 5-day backward trajectories calculated every 6 h along the cruise track. The top panel shows the July cruise from Incheon, Korea, to Nome Alaska, U.S.A., and the bottom panel shows the September cruise from Nome Alaska, U.S.A., to Busan, Korea. The color codes indicate the sections of the cruise track defined in Table 1. Green, red, blue, yellow, and violet correspond to sections I to IV in the top panel, and the same order of colors corresponds to sections VI to X in the bottom panel. (For interpretation of the references to colour in this figure legend, the reader is referred to the web version of this article.)

the Philippine Sea. Compared to the other sections, the backward trajectories in section II suggest little transport to the sampling position with air parcels originating from the nearby East Sea. During the cruise in section III, air parcels were transported from the northeast of the cruise track (Aleutian Islands), and in section IV, from the south of the cruise track (the open ocean of the North

Table 1
SHIPPO cruise track divided based on the origin of the air masses identified by the HYSPLIT 5-day backward trajectories and the statistical distribution of the CO and O_3 concentrations of each section.

Name	ID	Start	End	CO (ppbv)		O_3 (ppbv)	
				Mean	sd	Mean	sd
<Incheon – Nome>							
South Asia	I	7/13/2012 18:00	7/16/2012 12:00	144.9	66.2	31.8	12.6
Northern Japan	II	7/16/2012 12:00	7/19/2012 06:00	145.4	25.9	33.4	10.2
Aleutian Islands	III	7/19/2012 06:00	7/21/2012 18:00	107.4	25.0	24.6	4.9
North Pacific	IV	7/21/2012 18:00	7/25/2012 14:00	110.0	17.7	24.3	4.3
Siberia	V	7/25/2012 14:00	7/29/2012 20:20	103.0	9.3	21.7	4.6
<Nome – Busan>							
Arctic Sea/East Siberia	VI	9/11/2012 18:00	9/15/2012 18:00	127.5	1.3	28.3	4.0
Siberia/Okhotsk Sea	VII	9/15/2012 18:00	9/18/2012 15:00	127.3	4.1	26.1	3.1
North Pacific	VIII	9/18/2012 15:00	9/20/2012 06:00	109.7	33.9	24.5	17.0
Northern East Sea	IX	9/20/2012 06:00	9/22/2012 00:00	128.2	9.3	42.9	5.3
Korean Peninsula	X	9/22/2012 00:00	9/23/2012 00:00	179.6	17.8	62.7	5.7

Pacific). In section V, air parcels were dominantly passed through the Kamchatka Peninsula and far eastern Siberia.

During the September cruise, we encountered air parcels that were predominantly from the eastern Siberian subcontinent, except in section VIII. In section VI, air parcels were transported toward the south from the Arctic Ocean or from eastern Siberia. The characteristics of the backward trajectories in sections VII and VIII are clearly different. The former was transported from the free troposphere of eastern Siberia, and the latter from the marine boundary layer of the North Pacific. In both sections IX and X, air parcels were transported southward; in section IX, air parcels were passed over the East Sea, and in section X over the Korean Peninsula.

3. A 3-D global chemical transport model (MOZART-4) simulation

We used the MOZART-4 global chemical transport model to simulate the CO and O_3 concentrations along the cruise tracks. MOZART-4 contained more than 130 chemical and aerosol species and approximately 200 reactions and was driven by the Goddard Earth Observing System Model, Version 5 (GEOS-5) meteorology (Rienecker et al., 2008). In addition to the standard full chemistry model, we added tags for the sources (anthropogenic, biomass burning, biogenic, ocean, and chemical production) and for the emissions regions of CO, which allowed us to analyze the source composition and regional influence of CO. Fig. 2 illustrates tagged emission regions for anthropogenic and biomass burning sources (11 regions) and ocean sources (3 regions). Thus, a total of 27 tagged CO species were independently transported and reacted in the model. The model had a horizontal resolution of 1.9° × 2.5° and simulated up to 2 hPa, with 56 vertical levels. The chemical species were reacted and transported every 15 min in the model, and the results were averaged and recorded every 6 h. For the surface CO emission inventories, we used 2012's monthly emission of MACC/CityZEN EU projects (MACCity) (Lamarque et al., 2010) and the Fire INventory from the NCAR (FINN) (Wiedinmyer et al., 2011) dataset for anthropogenic and biomass burning sources, respectively. The monthly POET inventory (Olivier et al., 2003) for 2000 was used for biogenic and oceanic CO emissions.

4. Results and discussion

4.1. CO and O_3 observations

The CO and O_3 concentrations varied substantially during the

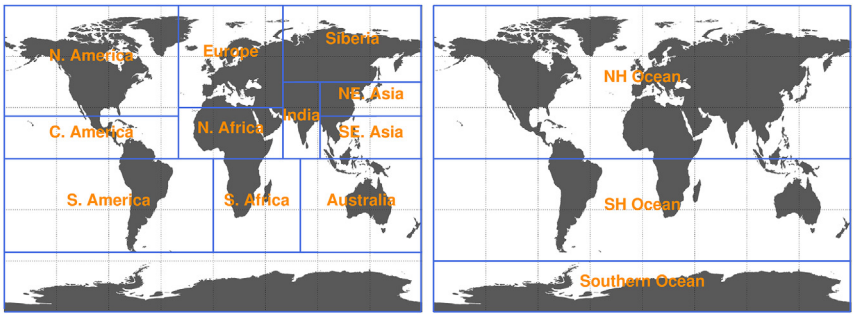

Fig. 2. CO source emission regions tagged in the MOZART-4 simulation. The 11 regions are tagged for anthropogenic and biomass burning sources (left panel), and the 3 regions are tagged for ocean sources (right panel).

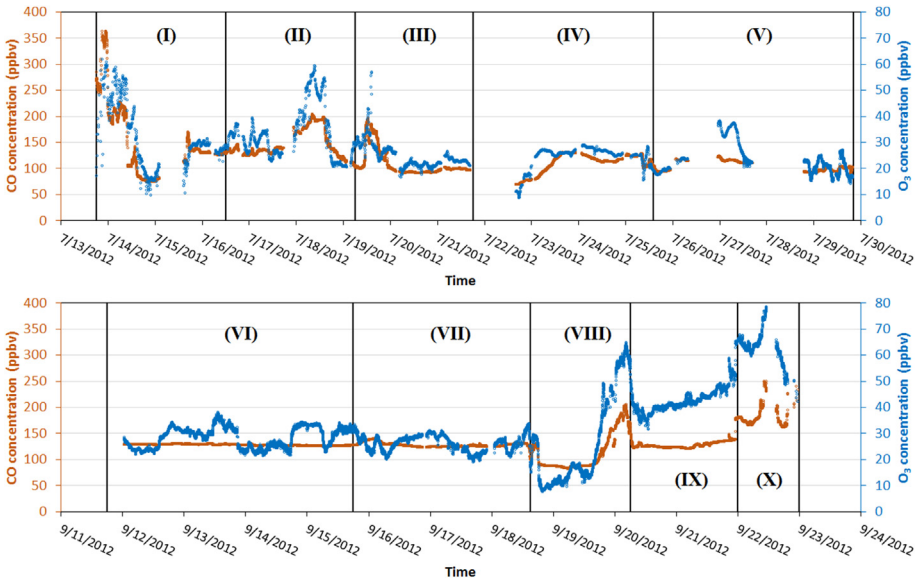

Fig. 3. CO (orange) and O_3 (blue) concentrations in the marine boundary layer along the cruise track. The upper and lower panels indicate two expeditions in July (Incheon – Nome, AK) and in September (Nome, AK – Busan), respectively. Note that the extended gaps in the July measurements result from data flagged for contamination by ship exhaust; refer to Fig. S2 for the complete measurements. (For interpretation of the references to colour in this figure legend, the reader is referred to the web version of this article.)

cruise (Fig. 3). In particular, the CO and O_3 concentrations observed in the area close to the Korean peninsula or Japan (sections I, II, VIII, and X in Fig. 3) fluctuated frequently, which is also demonstrated by the large standard deviation in Table 1. Those large CO and O_3 concentrations may be due to the anthropogenic emissions from northeastern Asian countries, China, Korea, and Japan, as suggested by the backward trajectory analyses (see Fig. 1).

While the CO varied as small as a few ppb over the Bering Sea (sections IV, V, VI and VII), the variation of O3 was as much as ~25 ppb. Since O_3 is predominantly formed and removed by photochemical reactions in the atmosphere, although these sections are far from the intense local sources such as urban (anthropogenic emission) or biomass burning area, the O_3 responded more sensitively than the CO in the remote regions. This implies that, for O_3, the ground emissions of its precursors would not be the sole factor controlling the O_3 concentrations in the regions, but instead that O_3 was possibly influenced by the input from the free troposphere or the lowermost stratosphere, as indicated by the backward trajectory analyses (see Fig. 1). This is explained in more detail in section 4.5 below.

In section IV, where air masses were transported from the central Pacific (Fig. 1), CO varied slightly (110.0 ± 17.7 ppbv), indicating that local sources should be far from that area and that the CO was well-mixed (Pfister et al., 2008). The concentration difference of ~20 ppb between section IV and V in July and section VI and VII in September is likely to be caused by the seasonal cycle of CO in the Bering Sea. Because approximately 90% of CO is removed by the CO + OH reaction, sunlight plays a central role in CO removal. This is also consistent with the CO trend observed at one of the NOAA GMD network stations (Novelli et al., 2003), Shemya Island station (52.71°N, 174.13°E), which is closest to the cruise track in the Bering Sea; the CO concentration during late July was 101.9 ppbv, increasing to 122.7 ppbv in September.

4.2. Comparison to model simulation

In Fig. 4, the 6-h mean concentrations of the modeled and observed CO and O_3 are compared in scatter plots. The model simulations were consistent with the observations in both CO ($r = 0.58$) and O_3 ($r = 0.43$) (see also Fig. S4). The model would have produced more realistic results if the data from sections I, IX and, X, near the Korean peninsula and Japan, were not included. The largest difference occurred in section I, probably because either the model did not properly account for the influence of air masses transported from the South China Sea or the emission rates of anthropogenic sources in the Northeast Asian countries would have been too strong to accurately predict. This is also supported by the CO data obtained at the site of Tae-Ahn (36.73°N, 126.13°E), one of the NOAA GMD network stations, nearby the cruise track, on July 2 and 19. The CO concentration was 166.5 ± 8.0 ppbv, which is close to the measured CO concentration in section I (144.9 ± 66.2 ppbv; Table 1).

Over the Northwestern Pacific and the Bering Sea (sections II to VIII), the model simulated the observations fairly well. The absolute mean differences between the model results and observations are 19.5 and 7.9 ppbv for CO and O_3, respectively. Over the Bering Sea (sections V and VI), where the model simulated the observations best among the cruise tracks, the differences in CO and O_3 are merely 0.9 and 8.2 ppbv in section V and −3.0 and 0.2 ppbv in section VI, despite the temporal difference of the two sections.

Fig. 5 shows the model-observation difference of CO and O_3. As one may expect, they show a robust correlation ($r = 0.82$). CH_4 and CO are major sources of tropospheric O_3 production in low NMHC environments, such as the free troposphere or the MBL, where our observations were conducted. Because we can assume a relatively constant CH_4 concentration in the observation regions, the positive correlation in Fig. 5 informs us that the errors in the modeled O_3 may come from the deviation of CO simulation from the observations. This is evident in that the model deviation for both CO and O_3 occurs where the model overestimated the CO concentrations, e.g., sections I, II, VIII, IX, and X.

4.3. CO source composition

Source contributions to the CO in the MBL along the cruise track were calculated using a tagging technique in MOZART-4 (Park et al., 2013; Pfister et al., 2008; Rienecker et al., 2011). A time series of the concentration from each source is shown in Fig. 6, and the relative source composition in each section is illustrated in Fig. 7.

Chemical production composes all of the CO produced by photochemical reactions in the troposphere, including the oxidation of CH_4 and NMHCs. This is the biggest source of CO in the troposphere (Duncan et al., 2007). In September, we found it predominant among the sources as its contribution was 65 ppbv on

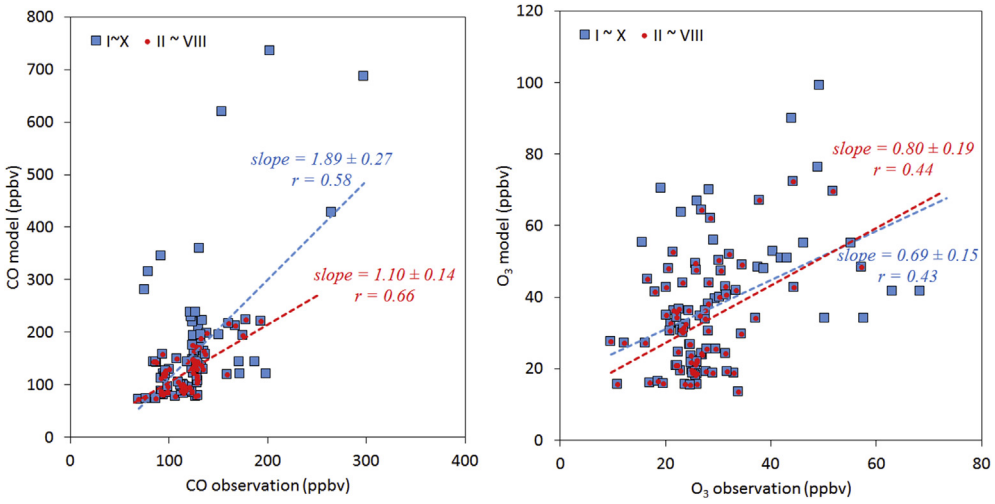

Fig. 4. Scatter plots between the observed and modeled CO and O_3 concentrations. Blue squares represent all of the 6-h mean data and red dots exclude the data from section I, IX and X that were strongly influenced by anthropogenic emissions. For both CO and O_3, the model results correspond better to the observations when the data from section I, IX and X are excluded. (For interpretation of the references to colour in this figure legend, the reader is referred to the web version of this article.)

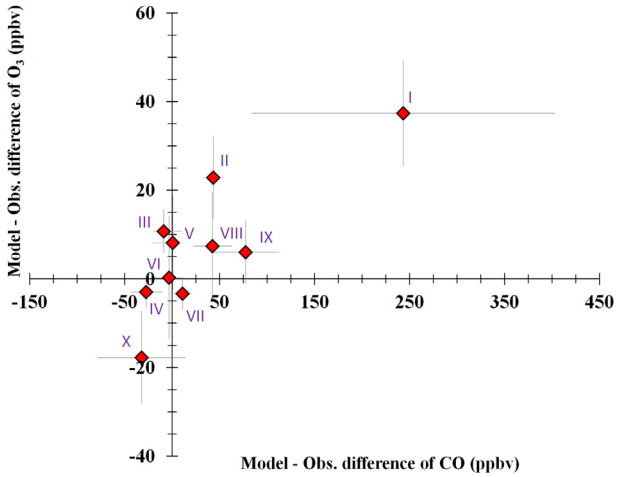

Fig. 5. Mean CO and O_3 concentration difference between the modeled and the observed data in each section. The correlation between the model-observation difference of CO and O_3 gives a correlation coefficient of 0.82. The error bars represent a 1-σ of the model-observation difference in each section.

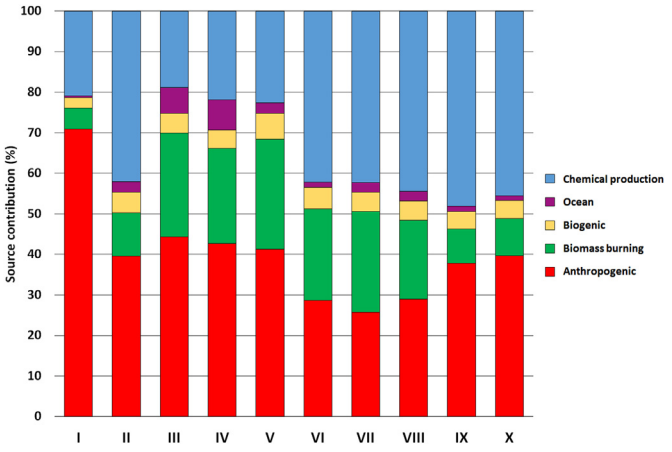

Fig. 7. Relative source strengths of CO in each section.

average. In July, when the photochemical destruction (CO + OH) was strong, its net contribution decreased and was quite different to anthropogenic emissions; the mean value of 83 ppbv from anthropogenic emissions exceeded chemical production by 45 ppbv.

The influence of anthropogenic emissions prevailed over Northeast Asia in both the July (sections I and II) and September cruises (sections IX and X). In particular, the CO in section I was predominantly composed of the anthropogenic sources.

During summer, Siberian boreal forest fires are usually frequent (van der Werf et al., 2010). Thus, the anthropogenic influence becomes weaker than emissions from biomass burning in eastern Siberia. The variability of anthropogenic sources decreased as *R/V Araon* sailed far from the source region, and biomass burning emissions appeared to govern the variation of the total CO concentration. Especially in section VI and VII, biomass burning contributes 23% and 25% of total CO, which are close to the

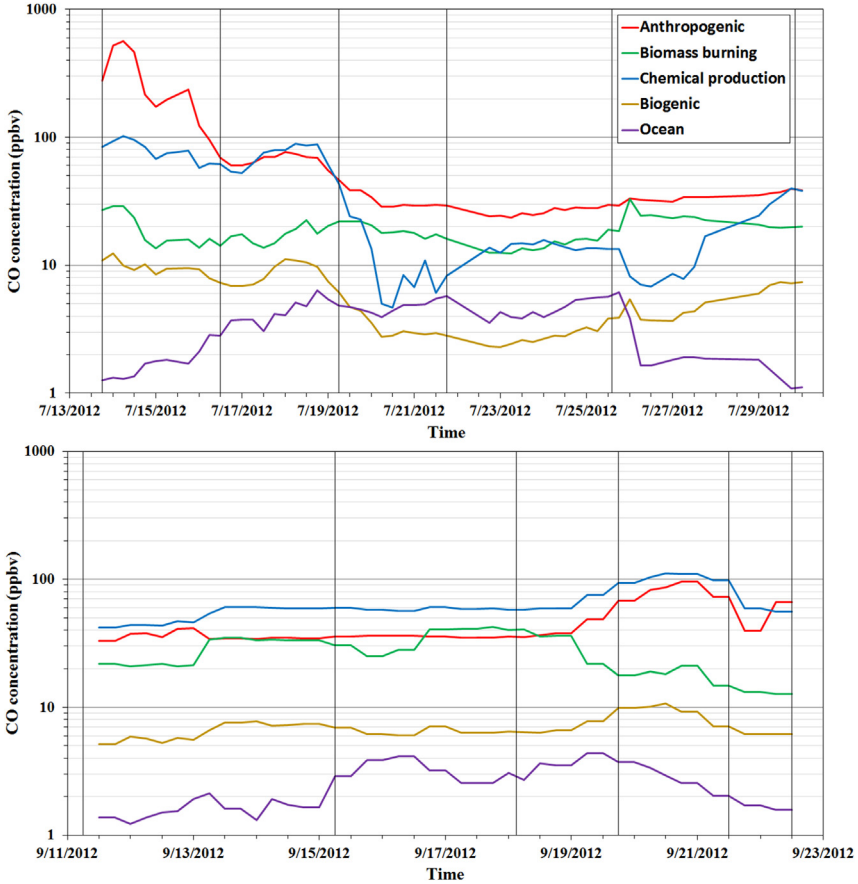

Fig. 6. Variation of the CO source composition that was calculated from the tagged MOZART-4 simulation. The upper panel is for the July cruise (Incheon – Nome, AK), and the bottom panel is for the September cruise (Nome, AK – Busan).

anthropogenic emissions of 29% and 26%, respectively.

In seawater, CO is produced by the photochemical oxidation of chromophoric dissolved organic matter. While the ocean has been known to be a minor source of tropospheric CO, the model simulation indicates that the air in the MBL of the open ocean (section III and IV in Fig. 7) contains oceanic CO up to 6–8 % of the total CO concentration. The substantial oceanic CO contribution is due to the minimum total CO concentration and strong oceanic CO production during summer (Olivier et al., 2003). Hence, within the MBL, we argue that the role of oceanic CO should not be neglected for understanding summer season CO-related chemistry.

4.4. Long-range transport of CO

Fig. 8 shows the relative contributions of CO source areas in terms of biomass burning, anthropogenic activities, and oceanic production. During the expedition, 54% of the CO from biomass burning originated from Siberian wild fires. Along with this, the contribution of Southeast Asian biomass burning comprised approximately 20% of the CO from biomass burning in the Northeast Asian area, which includes sections I, II, IX and X. North American biomass burning contributes as little as approximately 3%, on average, except near Alaska (sections V and VI), where 7% (section V) and 9% (section VI) of the total CO from biomass burning was derived from North America.

Anthropogenic CO from Northeast Asia prevailed along the ship track (59% on average). However, its influence decreased at higher latitudes. In sections V and VI, considerable amounts of anthropogenic CO were also transported from Europe and North America; the former contributed 26% and the latter 14% to the total anthropogenic CO. Nonetheless, Northeast Asia was the dominant source of anthropogenic CO in this area (35%).

We also analyzed CO sources transported from the Southern Hemisphere (SH). The anthropogenic emissions in the SH are fairly small, and one may expect a limited influence of SH anthropogenic CO during the cruise (Fig. 8). The model calculation indicates that 11% and 18% of the CO in sections I and X, respectively, originated from southern hemispheric biomass burning. Although the ocean is a minor source of tropospheric CO on a global scale, in sections I and X, where the cruise tracks are located in the lowest latitudes in July and September, respectively, oceanic CO transported from the SH was calculated to be 21% of total oceanic CO concentration, despite a two-month difference in the two sections. Therefore, this model calculation not only implies a notable amount of CO production in the SH ocean but also suggests its potentially important role in CO-related chemistry in the Northern Hemispheric MBL.

4.5. Analysis of the CO–O_3 relationship

Correlation between CO and O_3 may provide information about sources of air masses (Harris et al., 2000; Hirsch et al., 1996; Jaffe and Wigder, 2012; Kim et al., 2013; Parrish et al., 1993; Pfister et al., 2006). In remote regions where VOCs rarely exist, O_3 is mainly produced from photochemical reactions of CO and CH_4 when NOx concentrations are sufficiently high. Relatively lower O_3 concentrations can be observed near the sources of CO, but as an air mass ages, the O_3 concentration increases with the decreasing CO concentration. Additionally, the O_3 production rate can be estimated from the slope of the ratio of $[O_3]/[CO]$. Different than in the air mass aging process, negative CO–O_3 correlations could be observed when stratospheric O_3 is intruded to the troposphere or O_3 production is inhibited by NO in fresh pollution plumes (Lee and Feldstein, 2013).

Fig. 9 shows the observed CO–O_3 correlation in each section. The slopes range from 0.15 to 0.54 and are comparable to the values in the literature (Chin et al., 1994; Parrish et al., 1993). The relationships showed robust positive correlations (r = 0.62–0.96), except in sections VI, VII and X. This indicates, during the cruises, that the observed O_3 is likely to originate from the photochemical reactions of CO.

The slopes in sections I and X are 0.15 and 0.12, respectively. Because these regions are heavily influenced by Northeast Asian pollution, they showed lower slopes. Because the anthropogenic CO emissions prevail over NOx emissions in Northeastern Asia, this is a typical O_3 production rate in this area (Ding et al., 2009; Streets et al., 2006). Although the air masses in both sections IX and X

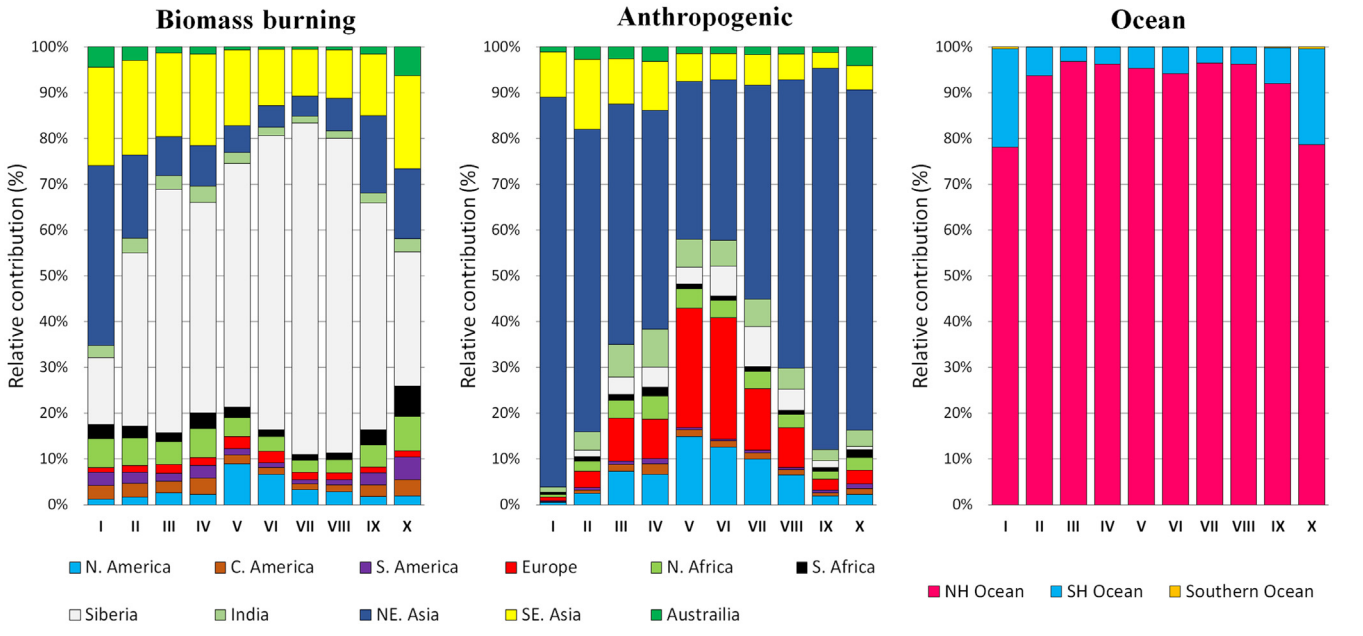

Fig. 8. Relative contribution of CO sources from various regions to the given section of the cruise track. For biomass burning and anthropogenic sources, 11 emission regions are traced and 3 regions are defined for ocean emissions in the model.

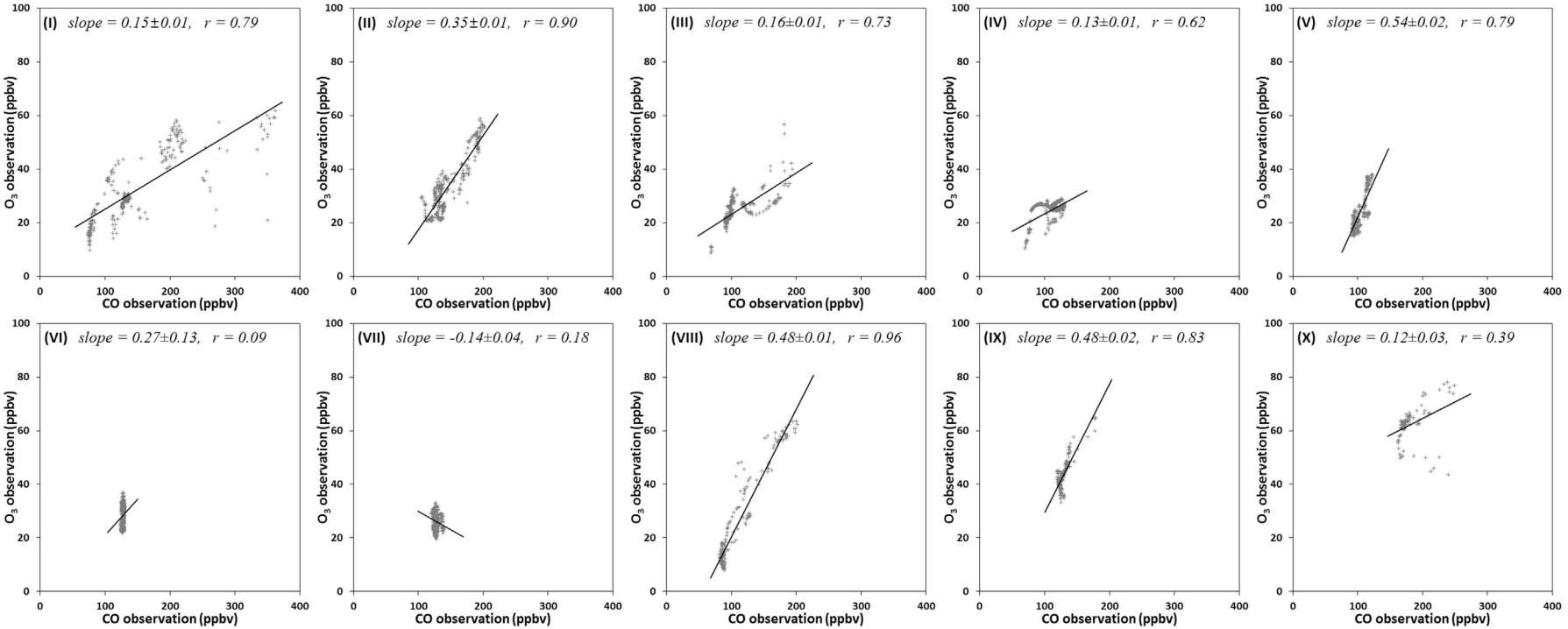

Fig. 9. Correlation between observed O_3 and CO in each section. Strong correlations can be seen in most of the sections, which could suggest that O_3 is mainly produced from photochemical reactions of CO. In section VI and VII, the correlations are distinctively different from the other sections, suggesting contributions of other O_3 sources, such as free troposphere or the lowermost stratosphere.

were transported southward from Northeastern China, the slope of section IX (0.48) is clearly different from that of section X (0.12). Five-day backward trajectories (Fig. 1) indicate that the air masses encountered in section IX passed through the Northern part of the East Sea, whereas those in section X blew over the Korean peninsula. This suggests that section X is more directly influenced by anthropogenic emissions than section IX.

The CO–O_3 correlation in sections VI and VII is distinctively different from the others. While the concentration of CO was almost constant, the O_3 concentration varied. Moreover, a negative slope is found in section VII as well as a weak correlation. This implies that the air masses in these sections have been transported away from the surface CO emission sources (i.e., the aged air masses were transported down from the free troposphere or the air masses were influenced by stratospheric O_3 intrusion). Because these sections are in a high latitude region, the tropopause heights are relatively low and the backward trajectories showed that the air masses were transported from relatively higher altitudes than the other sections (see Fig. 1).

In Fig. 10, the modeled CO–O_3 relationship in each section is compared to the observations. For most sections, the modeled and observed CO–O_3 slopes are laid closely onto the 1-to-1 line. However, for the sections VI, VII and IX, the observed CO–O_3 slopes are distinctly larger than the modeled slopes. Nevertheless, considering the large errors in the slopes of sections VI and VII, the modeled slopes do not substantially differ from the observations and suggest that the air masses are not influenced by the surface CO. Because section IX showed the second largest CO model-observation difference (Fig. 5), the lower slope of the modeled CO–O_3 relationship could be associated with the overestimated modeled CO. Moreover, the modeled slope close to 0 (-0.01 ± 0.06) implies that O_3 production from CO is inhibited by VOCs- or NO_x-related O_3 production in the model because our simulation results (Figs. 7 and 8) showed that this region is strongly influenced by Northeastern anthropogenic emissions. Thus, a more accurate modeling result can be acquired in section IX, when more realistic NOx and CO emission inventories and chemistries are developed and implemented in the model.

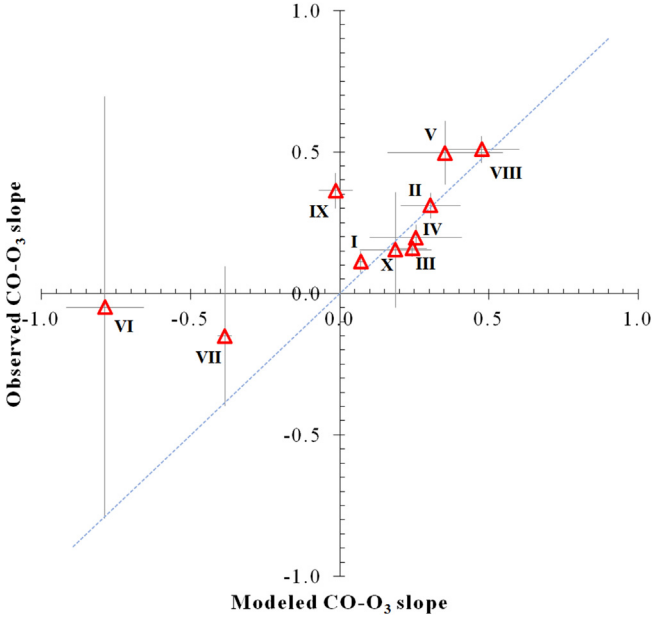

Fig. 10. A comparison of the slopes between the modeled and observed CO–O_3 relationship in each section. Six-hour mean concentrations were used in the analysis, and the error bars represent the standard error of the slopes. The 1-to-1 line is shown as a blue dotted line. (For interpretation of the references to colour in this figure legend, the reader is referred to the web version of this article.)

5. Summary and conclusions

As a part of the SHIPPO program, summer tropospheric CO and O_3 were continuously measured over the Northeastern Pacific, including the East Sea and the Bering Sea. Different sections of the cruise track revealed their characteristic variability. The CO and O_3 variabilities in each section ranged from 1 to 66 ppbv and 3–17 ppbv, respectively (see Table 1).

The CO-tagged MOZART-4 simulation provided useful insight regarding the origin and transport of observed chemical species. Model-observation differences occurred in the remote area – the Northeastern Pacific and the Bering Sea – suggesting that the biomass burning CO inventory needs to be updated, as this source played a central role in the CO concentration variations in the high northern latitudes. In the Northeastern Asia outflow region, a large model-observation difference was found. The elevated concentrations in MOZART-4 are somewhat affected by the overestimated biomass burning CO inventory as well. However because this area is influenced by numerous anthropogenic pollutants, including CO, NOx and NMHCs, a more detailed evaluation of anthropogenic CO emissions and a more accurate scheme of the chemical CO production should help to reduce the model-observation differences.

Anthropogenic emissions were a dominant source of CO in Northeastern Asia, and the relative importance of biomass burning increased in the higher latitude portion of the cruise track. The regional tagged CO revealed the anthropogenic CO composition over the Bering Sea region. In addition to Northeast Asian emissions, European and North American anthropogenic emissions also influence this region. In particular, the contribution of European anthropogenic emissions was comparable to Northeast Asia's.

In open ocean regions, the contribution of oceanic CO was up to 8% of the total CO concentration, and near the Korean peninsula, approximately 20% of oceanic CO was transported from the SH. Thus, the ocean is potentially an essential CO source of the MBL CO variations during the summer.

Positive correlations between CO and O_3 in the observations suggest that O_3 was likely formed by photochemical reactions from CO. However, this positive correlation was not sustained over the Bering Sea, associated with contributions of aged air masses transport from the free troposphere or possible downward transport of the lowermost stratospheric O_3. The modeled CO–O_3 relationship is generally consistent with the observations.

Acknowledgments

We acknowledge the captain and crew of the ice breaker *R/V Araon* for their on board assistance. This work was supported by Korea Polar Research Institute grants (PE13410, PM14040, and PP14020).

Appendix A. Supplementary data

Supplementary data related to this article can be found at http://dx.doi.org/10.1016/j.atmosenv.2015.04.015.

References

Arévalo-Martínez, D.L., Beyer, M., Krumbholz, M., Piller, I., Kock, A., Steinhoff, T., Körtzinger, A., Bange, H.W., 2013. A new method for continuous measurements of oceanic and atmospheric N_2O, CO and CO_2: performance of off-axis integrated cavity output spectroscopy (OA-ICOS) coupled to non-dispersive infrared detection (NDIR). Ocean Sci. 9, 1071–1087.

Bergamaschi, P., Hein, R., Heimann, M., Crutzen, P.J., 2000. Inverse modeling of the global CO cycle 1. Inversion of CO mixing ratios. J. Geophys. Res. 105, 1909–1927.

Brenninkmeijer, C.A.M., Röckmann, T., Bräunlich, M., Jöckel, P., Bergamaschi, P., 1999. Review of progress in isotope studies of atmospheric carbon monoxide. Chemosphere – Glob. Change Sci. 1, 33–52.
Buchmann, B., Brenninkmeijer, C., Klausen, J., Novelli, P.C., Penkett, S., Scheel, H.-E., Steele, P., Suda, K., Tarasova, O., Zellweger, C., 2010. Guidelines for the Measurement of Atmospheric Carbon Monoxide, GAW Research and Monitoring Reports. World Meteorological Organization Gloabl Atmospheric Watch.
Chin, M., Jacob, D.J., Munger, J.W., Parrish, D.D., Doddridge, B.G., 1994. Relationship of ozone and carbon monoxide over North America. J. Geophys. Res. Atmos. 99, 14565–14573.
Crutzen, P.J., Zimmermann, P.H., 1991. The changing photochemistry of the troposphere. Tellus Ser. A-Dynamic Meteorology Oceanogr. 43, 136–151.
Dickerson, R.R., Rhoads, K.P., Carsey, T.P., Oltmans, S.J., Burrows, J.P., Crutzen, P.J., 1999. Ozone in the remote marine boundary layer: a possible role for halogens. J. Geophys. Res. Atmos. 104, 21385–21395.
Ding, A., Wang, T., Xue, L., Gao, J., Stohl, A., Lei, H., Jin, D., Ren, Y., Wang, X., Wei, X., Qi, Y., Liu, J., Zhang, X., 2009. Transport of north China air pollution by mid-latitude cyclones: case study of aircraft measurements in summer 2007. J. Geophys. Res. Atmos. 114, D08304.
Draxler, R.R., Hess, G.D., 1998. An overview of the HYSPLIT_4 modeling system of trajectories, dispersion, and deposition. Aust. Meteor. Mag. 47, 295–308.
Duncan, B.N., Logan, J.A., Bey, I., Megretskaia, I.A., Yantosca, R.M., Novelli, P.C., Jones, N.B., Rinsland, C.P., 2007. Global budget of CO, 1988–1997: source estimates and validation with a global model. J. Geophys. Research-Atmospheres 112.
Edwards, D.P., Pétron, G., Novelli, P.C., Emmons, L.K., Gille, J.C., Drummond, J.R., 2006. Southern hemisphere carbon monoxide interannual variability observed by Terra/Measurement of pollution in the Troposphere (MOPITT). J. Geophys. Res. Atmos. 111, D16303.
Ehhalt, D., Prather, M., Dentener, F., Derwent, R., Dlugokencky, E., Holland, E., Isaksen, I., Katima, J., Kirchhoff, V., Matson, P., Midgley, P., Wang, M., 2001. Climate Change 2001: the Scientific Basis (Atmospheric Chemistry and Greenhouse Gases). Intergovernmental Panel on Climate Change Third Assessment Report Cambridge University Press, Cambridge, UK.
Emmons, L.K., Walters, S., Hess, P.G., Lamarque, J.F., Pfister, G.G., Fillmore, D., Granier, C., Guenther, A., Kinnison, D., Laepple, T., Orlando, J.J., Tie, X., Tyndall, G., Wiedinmyer, C., Baughcum, S.L., Kloster, S., 2010. Description and evaluation of the model for Ozone and related chemical Tracers, version 4 (MOZART-4). Geosci. Model Dev. 3, 43–67.
Harris, J.M., Dlugokencky, E.J., Oltmans, S.J., Tans, P.P., Conway, T.J., Novelli, P.C., Thoning, K.W., Kahl, J.D.W., 2000. An interpretation of trace gas correlations during Barrow, Alaska, winter dark periods, 1986–1997. J. Geophys. Res. Atmos. 105, 17267–17278.
Hauglustaine, D.A., Brasseur, G.P., Walters, S., Rasch, P.J., Muller, J.F., Emmons, L.K., Carroll, C.A., 1998. MOZART, a global chemical transport model for ozone and related chemical tracers 2. Model results and evaluation. J. Geophys. Research-Atmospheres 103, 28291–28335.
Heard, D.E., Read, K.A., Methven, J., Al-Haider, S., Bloss, W.J., Johnson, G.P., Pilling, M.J., Seakins, P.W., Smith, S.C., Sommariva, R., Stanton, J.C., Still, T.J., Ingham, T., Brooks, B., De Leeuw, G., Jackson, A.V., McQuaid, J.B., Morgan, R., Smith, M.H., Carpenter, L.J., Carslaw, N., Hamilton, J., Hopkins, J.R., Lee, J.D., Lewis, A.C., Purvis, R.M., Wevill, D.J., Brough, N., Green, T., Mills, G., Penkett, S.A., Plane, J.M.C., Saiz-Lopez, A., Worton, D., Monks, P.S., Fleming, Z., Rickard, A.R., Alfarra, M.R., Allan, J.D., Bower, K., Coe, H., Cubison, M., Flynn, M., McFiggans, G., Gallagher, M., Norton, E.G., O'Dowd, C.D., Shillito, J., Topping, D., Vaughan, G., Williams, P., Bitter, M., Ball, S.M., Jones, R.L., Povey, I.M., O'Doherty, S., Simmonds, P.G., Allen, A., Kinnersley, R.P., Beddows, D.C.S., Dall'Osto, M., Harrison, R.M., Donovan, R.J., Heal, M.R., Jennings, S.G., Noone, C., Spain, G., 2006. The North Atlantic Marine boundary layer experiment (NAMBLEX). Overview of the campaign held at Mace Head, Ireland, in summer 2002. Atmos. Chem. Phys. 6, 2241–2272.
Hirsch, A.I., Munger, J.W., Jacob, D.J., Horowitz, L.W., Goldstein, A.H., 1996. Seasonal variation of the ozone production efficiency per unit NO_x at Harvard Forest, Massachusetts. J. Geophys. Res. Atmos. 101, 12659–12666.
IPCC, 2007. Climate change 2007: the physical science basis. In: Solomon, S., Qin, D., Manning, M., Chen, Z., Marquis, M., Averyt, K.B., Tignor, M., Miller, H.L. (Eds.), Contribution of Working Group I to the Fourth Assessment Report of the Intergovernmental Panel on Climate Change. Cambridge University Press, Cambridge United Kingdom and New York, NY, USA.
Jaffe, D.A., Wigder, N.L., 2012. Ozone production from wildfires: a critical review. Atmos. Environ. 51, 1–10.
Kim, P.S., Jacob, D.J., Liu, X., Warner, J.X., Yang, K., Chance, K., Thouret, V., Nedelec, P., 2013. Global ozone–CO correlations from OMI and AIRS: constraints on tropospheric ozone sources. Atmos. Chem. Phys. 13, 9321–9335.
Kistler, R., Collins, W., Saha, S., White, G., Woollen, J., Kalnay, E., Chelliah, M., Ebisuzaki, W., Kanamitsu, M., Kousky, V., van den Dool, H., Jenne, R., Fiorino, M., 2001. The NCEP–NCAR 50–Year reanalysis: monthly means CD–ROM and documentation. Bull. Am. Meteorological Soc. 82, 247–267.
Lamarque, J.-F., Bond, T.C., Eyring, V., Granier, C., Heil, A., Klimont, Z., Lee, D., Liousse, C., Mieville, A., Owen, B., Schultz, M.G., Shindell, D., Smith, S.J., Stehfest, E., Van Aardenne, J., Cooper, O.R., Kainuma, M., Mahowald, N., McConnell, J.R., Naik, V., Riahi, K., van Vuuren, D.P., 2010. Historical (1850–2000) gridded anthropogenic and biomass burning emissions of reactive gases and aerosols: methodology and application. Atmos. Chem. Phys. 10, 7017–7039.
Lee, S., Feldstein, S.B., 2013. Detecting ozone- and greenhouse Gas–Driven wind trends with observational data. Science 339, 563–567.
Novelli, P.C., Masarie, K.A., Lang, P.M., Hall, B.D., Myers, R.C., Elkins, J.W., 2003. Reanalysis of tropospheric CO trends: effects of the 1997–1998 wildfires. J. Geophys. Res. 108.
Olivier, J., Peters, J., Granier, C., Petron, G., Müller, J.F., Wallens, S., 2003. Present and Future Surface Emissions of Atmospheric Compounds. POET report #2 .EU project EVK2-1999-00011.
Park, K., Emmons, L.K., Wang, Z., Mak, J.E., 2013. Large interannual variations in nonmethane volatile organic compound emissions based on measurements of carbon monoxide. Geophys. Res. Lett. 40, 221–226.
Parrish, D.D., Holloway, J.S., Trainer, M., Murphy, P.C., Fehsenfeld, F.C., Forbes, G.L., 1993. Export of North American ozone pollution to the North Atlantic Ocean. Science 259, 1436–1439.
Pfister, G., Hess, P.G., Emmons, L.K., Lamarque, J.F., Wiedinmyer, C., Edwards, D.P., Pétron, G., Gille, J.C., Sachse, G.W., 2005. Quantifying CO emissions from the 2004 Alaskan wildfires using MOPITT CO data. Geophys. Res. Lett. 32, L11809.
Pfister, G.G., Emmons, L.K., Hess, P.G., Honrath, R., Lamarque, J.F., Val Martin, M., Owen, R.C., Avery, M.A., Browell, E.V., Holloway, J.S., Nedelec, P., Purvis, R., Ryerson, T.B., Sachse, G.W., Schlager, H., 2006. Ozone production from the 2004 North American boreal fires. J. Geophys. Res. Atmos. 111, D24S07.
Pfister, G.G., Emmons, L.K., Hess, P.G., Lamarque, J.F., Orlando, J.J., Walters, S., Guenther, A., Palmer, P.I., Lawrence, P.J., 2008. Contribution of isoprene to chemical budgets: a model tracer study with the NCAR CTM MOZART-4. J. Geophys. Res. 113, D05308.
Rienecker, M.M., Suarez, M.J., Gelaro, R., Todling, R., Bacmeister, J., Liu, E., Bosilovich, M.G., Schubert, S.D., Takacs, L., Kim, G.-K., Bloom, S., Chen, J., Collins, D., Conaty, A., da Silva, A., Gu, W., Joiner, J., Koster, R.D., Lucchesi, R., Molod, A., Owens, T., Pawson, S., Pegion, P., Redder, C.R., Reichle, R., Robertson, F.R., Ruddick, A.G., Sienkiewicz, M., Woollen, J., 2011. MERRA: NASA's Modern-Era retrospective analysis for research and applications. J. Clim. 24, 3624–3648.
Rienecker, M.M., Suarez, M.J., Todling, R., et al., 2008. The GEOS-5 Data Assimilation System – Documentation of Versions 5.0.1, 5.1.0, and 5.2.0. Technical Report Series on Global Modeling and Data Assimilation, 27.
Sanhueza, E., Dong, Y., Scharffe, D., Lobert, J.M., Crutzen, P.J., 1998. Carbon monoxide uptake by temperate forest soils: the effects of leaves and humus layers. Tellus Ser. B-Chemical Phys. Meteorology 50, 51–58.
Shim, C., Li, Q., Luo, M., Kulawik, S., Worden, H., Worden, J., Eldering, A., Diskin, G., Sachse, G., Weinheimer, A., Knapp, D., Montzca, D., Campos, T., 2009. Satellite observations of Mexico city pollution outflow from the Tropospheric Emissions Spectrometer (TES). Atmos. Environ. 43, 1540–1547.
Stevenson, D.S., Dentener, F.J., Schultz, M.G., Ellingsen, K., van Noije, T.P.C., Wild, O., Zeng, G., Amann, M., Atherton, C.S., Bell, N., Bergmann, D.J., Bey, I., Butler, T., Cofala, J., Collins, W.J., Derwent, R.G., Doherty, R.M., Drevet, J., Eskes, H.J., Fiore, A.M., Gauss, M., Hauglustaine, D.A., Horowitz, L.W., Isaksen, I.S.A., Krol, M.C., Lamarque, J.F., Lawrence, M.G., Montanaro, V., Müller, J.F., Pitari, G., Prather, M.J., Pyle, J.A., Rast, S., Rodriguez, J.M., Sanderson, M.G., Savage, N.H., Shindell, D.T., Strahan, S.E., Sudo, K., Szopa, S., 2006. Multimodel ensemble simulations of present-day and near-future tropospheric ozone. J. Geophys. Res. Atmos. 111, D08301.
Streets, D.G., Zhang, Q., Wang, L., He, K., Hao, J., Wu, Y., Tang, Y., Carmichael, G.R., 2006. Revisiting China's CO emissions after the transport and chemical evolution over the Pacific (TRACE-P) mission: synthesis of inventories, atmospheric modeling, and observations. J. Geophys. Res. Atmos. 111, D14306.
van der Werf, G.R., Randerson, J.T., Giglio, L., Collatz, G.J., Mu, M., Kasibhatla, P.S., Morton, D.C., DeFries, R.S., Jin, Y., van Leeuwen, T.T., 2010. Global fire emissions and the contribution of deforestation, savanna, forest, agricultural, and peat fires (1997–2009). Atmos. Chem. Phys. 10, 11707–11735.
Weinstock, B., Niki, H., 1972. Carbon monoxide balance in nature. Science 176, 290–292.
Wiedinmyer, C., Akagi, S.K., Yokelson, R.J., Emmons, L.K., Al-Saadi, J.A., Orlando, J.J., Soja, A.J., 2011. The Fire Inventory from NCAR (FINN): a high resolution global model to estimate the emissions from open burning. Geosci. Model Dev. 4, 625–641.
Zellweger, C., Steinbacher, M., Buchmann, B., 2012. Evaluation of new laser spectrometer techniques for in-situ carbon monoxide measurements. Atmos. Meas. Tech. 5, 2555–2567.